Measurement Techniques

Comparison between precipitation estimates of ground-based weather radar composites and GPM's DPR rainfall product over Germany

Velibor Pejcic[1*], Pablo Saavedra Garfias[2], Kai Mühlbauer[1], Silke Trömel[1,3] and Clemens Simmer[1,3]

[1]Institute for Geosciences, Section Meteorology, University of Bonn, Bonn, Germany
[2]Geophysical Institute, University of Bergen, Bergen, Norway
[3]Laboratory for Clouds and Precipitation Exploration, Geoverbund ABC/J, Bonn, Germany

Abstract

We compare more than three years (between 2014 and 2018) of precipitation estimates over Germany from the Dual-frequency Precipitation Radar (DPR) operating on the core satellite of the Global Precipitation Mission (GPM) with the radar-derived precipitation product RADOLAN RY provided by the German national meteorological service (DWD, Deutscher Wetterdienst). Incomplete overlap between the observation volumes due to the different scan geometries and inconsistencies related to the mutually assumed hydrometeor phases lead to large differences, when directly comparing DPR's near surface product (DPRns) with RADOLAN RY. We improve the correspondence between both data sets via two steps. First, we derive an adjusted DPR near surface product (DPRans) extracted from the DPR vertical profiles, that best fits to the scans height and beam width of the surface radar observations. Second, the data is classified into liquid, solid and mixed phases by adjusting hydrometeor phase classification (aHPC) to the RADOLAN scan geometry. With these steps the correlation between both data sets increases from $r = 0.49$ to $r = 0.61$ and the RMSD is reduced from 2.94 mm/h to 1.83 mm/h for the commonly observed precipitation, exceeding most of the results found in previous studies. The agreement is best in stratiform precipitation ($r = 0.68$, RMSD = 1.4 mm/h), for only stratiform and summer season ($r = 0.7$, RMSD = 1.59 mm/h), and for stratiform with only liquid precipitation ($r = 0.67$, RMSD = 1.58 mm/h). Unlike the the standard DPRns, the new DPRans product exhibits almost no seasonal differences in the capability of detection; for all seasons the CSI is 0.94 and the FAR/IFAR are 0.04/0.02.

Keywords: GPM DPR, RADOLAN, satellite rain rate, surface precipitation

1 Introduction

The Global Precipitation Measurement (GPM) mission is a constellation of satellites, that provide global observations of rain and snow. GPM's central objective is to improve our understanding of the global water cycle and its connection to climate change, mesoscale dynamics and storm structures, and to gain new insights into microphysical processes (Hou et al., 2014). The GPM core satellite, a joint effort of the National Aeronautics and Space Administration (NASA) and the Japan Aerospace Exploration Agency (JAXA) launched into orbit on February 2014, is the successor for the Tropical Rainfall Measuring Mission (TRMM; Simpson et al., 1988) and the second satellite in space carrying a precipitation radar. While TRMM observations were restricted to the tropical/subtropical belt, GPM allows for almost global observations. The GPM core satellite payload comprises two main instruments: the conical-scanning multi-channel (10–183 GHz) microwave imager (GMI) and the dual-frequency Ka-band (35.5 GHz)

and Ku-band (13.5 GHz) Precipitation Radar (DPR). The satellite with a non-sun-synchronous low earth orbit (LEO) of around 400 km allows for observations over a much wider latitude belt between 65° North and 65° South compared to TRMM.

GMI and its DPR are especially suited for the detection of light precipitation and snow, which are quite common at mid and high latitudes (Skofronick-Jackson et al., 2017). The wider coverage of the GPM core satellite fills the large observational gaps for precipitation over oceans and areas with low-density or non-existing surface networks, and thus has the potential to improve climatological datasets and to provide valuable observations for numerical weather forecasting (Conrick and Mass, 2019) and hydrological and global climate modeling. GPM observations are also helpful for flood and extreme weather detection and very important for global-scale hazard frameworks (Kirschbaum et al., 2012; Wu et al., 2012; Hou et al., 2014). Warren et al. (2018) show that DPR observations have also some potential to serve as a calibration standard for distributed ground-based precipitation radars. Louf et al. (2019) and Crisologo et al. (2018) enhanced the con-

*Corresponding author: Velibor Pejcic, Institute for Geosciences, Section Meteorology, University of Bonn, Auf dem Hügel 20, 53121 Bonn, e-mail: velibor@uni-bonn.de
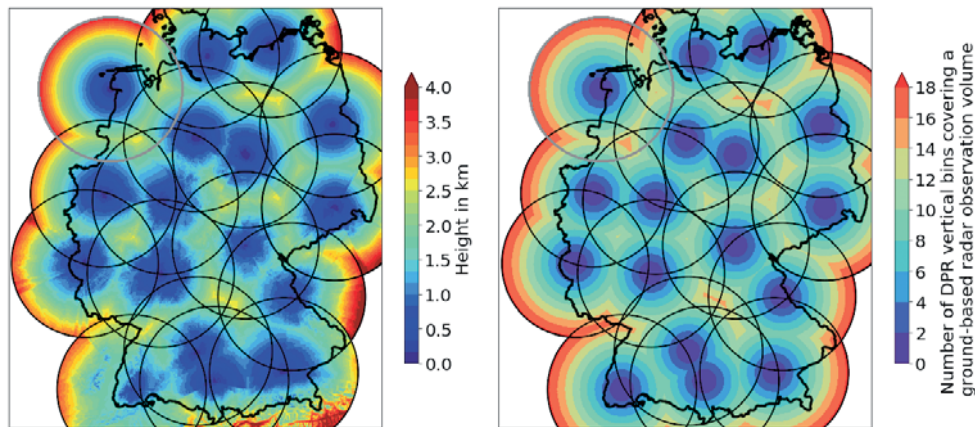
Figure 1: C-band precipitation Doppler radar network of DWD. The circles are the maximum radar ranges. The grey circles represent single-pol radars. The left image shows in color the range bin heights above ground in km. The right image shows in color the number of vertical GPM-DPR range bins contained within a single RY bin.

sistency of this calibration and increased its accuracy. Similarly, GMI's brightness temperature measurements are used as an inter-satellite calibration standard for passive microwave radiometers (PMR) on other satellites (NEECK et al., 2014).

A wide variety of precipitation products are obtained from the single/dual frequency radar observations, passive observations or combined active-passive observations. Both single-frequency and dual-frequency rain retrievals (LIAO et al., 2014; IGUCHI et al., 2000) from the core satellite are provided as standard products. Retrievals with the Goddard Profiling Algorithm GPROF algorithm (KUMMEROW et al., 2015) and the GPM combined algorithm are based on both the core satellite's GMI and DPR observations (GRECU et al., 2016). These multi-sensor precipitation retrieval methods are applied to the whole GPM satellite constellation in order to generate the global Integrated Multi-satellitE Retrievals for GPM (IMERG, HUFFMAN et al., 2015; TAN et al., 2019).

GPM-based precipitation retrievals are usually evaluated by comparison with ground-based measurements. Since the launch of the TRMM satellite many such comparisons have been performed, although restricted to the tropics and subtropics e.g. over West Africa (NICHOLSON et al., 2003), South America (ROZANTE et al., 2010), Korea (PARK et al., 2015), Australia (DEO et al., 2018), and the United States (WOLFF et al., 2005; LIAO and MENEGHINI, 2009). Comparisons with precipitation gauges and reanalysis data yield good agreements, particularly for cases with observations below the melting layer, over oceans, over flat terrain, and for stratiform precipitation (CANNON et al., 2017; SPEIRS et al., 2017; PETRACCA et al., 2018).

Products derived from observations of the GPM core satellite allow for extended ground evaluations compared to TRMM because of GPM's additional radar frequency and higher inclination orbit leading to a wider range of observed climate regions. Ground validation systems were established to support the development and evaluation of the GPM core satellite algorithms in

the pre- and post-launch era, and have been specifically designed for individual ground-based weather radars networks (SCHWALLER and MORRIS, 2011; KIM et al., 2014). LE et al. (2016) report about a DPR post-launch evaluation over the United States of America with weather radars from NEXRAD and TRMM products. Field campaigns like the NASA Olympic Mountains Ground Validation Experiment (OLYMPEX; HOUZE et al., 2015), Iowa Flood Studies (IFloodS, CHEN et al., 2017; NAYAK et al., 2016) and the Integrated Precipitation and Hydrology Experiment (IPHEx, BARROS et al., 2014) contributed to these efforts with multi-sensor observations at the ground and from aircraft in order to assess the performance of satellite estimates over different terrain types and for various precipitation regimes.

Over Europe only few studies are available. E.g. PETRACCA et al. (2018) evaluate the DPR liquid rain near-surface products over complex terrain in Italy and found an overall correlation of r = 0.44 with uncertainties increasing with terrain elevation and a higher quality of rain estimates during warm compared to cold periods. Investigations in complex terrain in Switzerland (SPEIRS et al., 2017) revealed that in addition to surface elevation the terrain unevenness also contributes to inaccuracies of GPM products. Similar to PETRACCA et al. (2018) they found higher correlations between ground-based and satellite-based estimates for liquid phase precipitation (r = 0.796) and during summer (r = 0.658) compared to solid precipitation (r = 0.521) and during winter (r = 0.57). WATTERS et al. (2018) report similar findings, but noted that misinterpretations of the bright band as clutter could lead to an underestimation of the DPR derived rain rates, and that the accuracy of the estimated bright-band height from DPR profiles plays an important role in the estimation of near-surface precipitation. For stratiform events its estimation error was found to be on the order of 125 m compared to in-situ radar measurements. Comparisons with freezing level heights derived from re-analyses showed even better agreements (CANNON et al., 2017).

Despite extensive research on the different sources of uncertainties in previous studies, there is still a lack of knowledge regarding the effects introduced by phase miss-classification and spatial mismatches between the so-called DPR near surface product (DPRns) and the ground-based precipitation estimates due to the different scanning geometries performed by both system types. Here, we compare the latest version (V05) of the DPR precipitation estimates with three years of the Germany-wide near-surface precipitation product RADOLAN of the German national meteorological service (DWD, *Deutscher Wetterdienst*). The DWD offers a wide variety of different radar products that are widely used for research on hydrology (WINTERRATH et al., 2012; FISCHER et al., 2016; AUERSWALD et al., 2019), data assimilation (MILAN et al., 2008) and climate (WINTERRATH et al., 2018; JUNGHÄNEL et al., 2016; PSCHEIDT et al., 2019; LENGFELD et al., 2019). We focus on the RY composite product derived from the so-called precipitation scans of the weather radar network. This product is generated only from archived operational radar data and is not the climatological data used in AUERSWALD et al. (2019). RY allows a more detailed quantification on uncertainties between pure radar observations. The precipitation scans follow the orography to avoid terrain-caused beam blocking, hence the observations used for RY originate from different heights and have varying sampling volumes depending on the distance from a particular radar to its range bins used, which should to be taken into account when comparing with the commonly-used near-surface product provided by DPR V05 (Section 2). We first quantify the uncertainties by directly comparing the DPR near-surface product (DPRns) with the upscaled RY product, but suggest a better suited DPR product spatially adjusted to the upscaled RY (DPRans). We examine the quality of the matching for different orographic, synoptic, and microphysical (hydrometeor types) influences, and for non-uniform hydrometeor-phase beam-filling effects (Section 3). The results are summarized and discussed in Section 4.

2 Data and Methods

2.1 DPR products

The DPR measures vertical profiles of radar reflectivity at Ku and at Ka band with footprints of about 5 km in diameter. The Ku-band radar scans across orbit with a swath width of 245 km resolved in 49 footprints for the so-called Normal Scan (NS) with a vertical resolution of 125 m. The Ka-band scans a smaller swath of 120 km also with 49 footprints but separated into two scan types: the Matched Scan (MS) contains 25 footprints exactly overlapping the footprints of the innermost 25 footprints of the NS and has a vertical resolution of 125 m; the 24 footprints of the High Sensitivity Scan (HS) are shifted along-scan by half a footprint relative to the MS (see Figure 2.2-2 in IGUCHI et al., 2017)

and are designed for light rain and snow detection by operating in a high-sensitivity mode with a reduced vertical resolution of 250 m (FURUKAWA et al., 2013).

The different scans allow for both single- (SF) and dual-frequency (DF) precipitation retrievals. For footprints containing both frequencies bright-band detection (altitude and thickness), precipitation phase classification (solid, mixed, liquid), and precipitation type (stratiform, convective) are derived following LE et al. (2016), LE and CHANDRASEKAR (2013) and AWAKA et al. (2016). Parameters of the drop size distribution (DSD) and derived precipitation rates are estimated from the dual-frequency ratio (DFR) following SETO et al. (2013). For SF retrievals, especially for the outer swath footprints of the NS, precipitation type and bright band height are estimated with the TRMM method (AWAKA et al., 1997; AWAKA et al., 2016), and DSD parameters are estimated from the ratio of reflectivity to specific attenuation following SETO et al. (2013). Classifications and retrievals are performed from the uppermost level of detected reflectivity (storm top height, STH) to the lowest level not contaminated with ground clutter (clutter-free bottom, CFB). Reported precipitation rates below the CFB (typically around 0.9 km above ground) are extrapolated values above the CFB estimates (AWAKA et al., 2016; IGUCHI et al., 2017).

We evaluate in this study the dual-frequency normal scan (DF NS) product (file specification 2ADPR, IGUCHI and MENEGHINI, 2019), which consists of dual-frequency rain retrievals in the inner swath and single-frequency rain retrievals in the outer swath. 2ADPR data files include the vertical profiles of the precipitation rate estimates (variable name precipRate) and the hydrometeor phase (variable name phase), and a near-surface precipitation rate estimate (variable name precipRate-NearSurface; in the following termed DPRns) which is the precipitation rate estimated at the first bin above the clutter free bottom (CFB) height.

2.2 RADOLAN RY product

RADOLAN-RY (Radar online adjustment, RADar On-Line ANeichung, in the following abbreviated by RY) is the DWD procedure to derive radar-based composite precipitation products from the 17 C-band radars covering Germany (16 dual-pol and one single-pol radar located in the northwestern area (Emden, Figure 1 grey circle) at a 1 km spatial resolution grid and five minutes temporal resolution (Figure 1, left). An adjustment to rain gauges – as suggested in the acronym RADOLAN – is only carried out for an hourly product and not for the RY product. All radars perform the so-called precipitation scan with an azimuthal resolution of 1° and a range resolution of 250 m with an orography-following elevation angle (0.5°–1.8°). For the RADOLAN RY procedure, however, 1 km range resolution is provided. RY rain rates are based on a radar reflectivity-dependent z-R relationships derived for liquid hydrometeors, which are applied to the observed
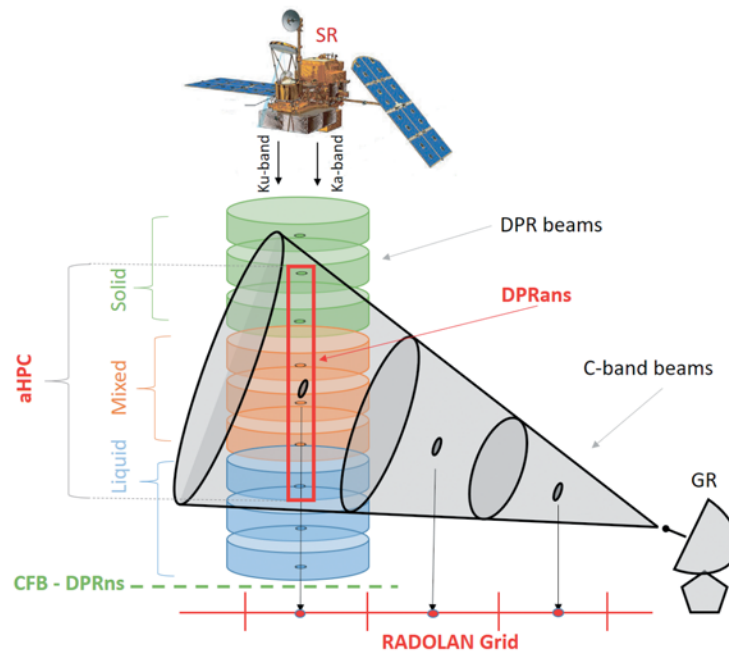
Figure 2: Schematic representation depicting the averaging procedure for generating the DPR adjusted near surface product (DPRans) from the DPR column-resolved rain rate estimates (DPR beams) encompassing the ground-based radar beam from which the RADOLAN RY product is generated. In gray the pre-composite ground-based radar observation geometry is shown. The horizontal red line indicates its spatial grid and thus the center points of the RY composite. The colored cylinders represent the quasi-horizontal DPR range bins with the color indicating their precipitation phase. The bins used for the construction of the DPRans rain rate and the hydrometeor phase product are indicated within the vertical red rectangle. The clutter free bottom (CFB) (estimated height of DPRns) is shown with a dashed green horizontal line. GPM picture modified from HOU et al. (2014)

radar reflectivity after clutter- and beam blockage-corrections (BARTELS et al., 2004; https://www.dwd.de/DE/leistungen/radolan/radolan.html). Over regions with overlapping observations from different radars the decisive criteria for the choice of the bins in the overlapped area is the quality of the measurement, in cases where the quality is comparable then the maximum reflectivity is used. Since 31.08.2016, a weighted average instead of the maximum is used, which depends on the distance to the involved radars (DEUTSCHER WETTERDIENST, 2020). The mean height and mean beam width (Figure 1, right) of an observation entering the radar composite can be estimated from the elevation angle of the respective observing radar. Heights may vary slightly when the respective measurement is contaminated by clutter (personal conversations with DWD and MeteoSolution, 2019).

2.3 Generation of matching observations

For the statistical comparison of both observation types, we average the horizontally higher-resolved ground-based radar observations over the DPR footprints using weights defined by the DPR antenna gain following WATTERS et al. (2018). The module Zonal Statistics contained in the open source library wradlib (HEISTERMANN and PFAFF, 2013), which is used in this study, finds all RY pixels corresponding to one DPR footprint and calculates the RY value upscaled to the same resolution

as DPR, hereafter referred to as RYups. Since the RY estimates are available every 5 minutes, the maximum temporal difference to the closest (irregularly observed) DPRns observation is 2.5 minutes.

In order to further reduce sampling-based discrepancies (will be discussed in detail in Section 2.4) between RYups and DPRns (Figure 2, green dashed line versus black dots), we construct an adjusted dataset named DPRans (DPR adjusted near surface product, Figure 2, red box) from the DPR vertical profiles, which is adapted to the RYups mean beam height and width (cone starting at the ground-based radar in Figure 2). For each DPR footprint, DPRans rain rates are averaged (BISWAS and CHANDRASEKAR, 2018; D'ADDERIO et al., 2018) over that DPR profile sector, which embraces the RYups radar volume (red frame inside DPR field of view in Figure 2). Heights and beam propagation for the ground-based and space-borne radar are calculated following IGUCHI et al. (2017). Figure 2 illustrates a case, when a single ground-based radar bin encompasses a set of DPR vertical range bins with a variety of hydrometeor phases. Every DPR bin has a precipitation rate estimated according to its phase. RYups and DPRans pixels each comprises one rain rate value and a percentage of different precipitation phases inside that pixel. Therefore, a simple subdivision into different precipitation phases similar to DPRns's standard phase product which only represents the hydrometeor phase of the first DPR bin over the CFB, cannot be done.

Figure 1 (right panel) indicates that a single ground-based radar bin (and thus the corresponding RYups estimate) may encompass up to 18 DPR vertical bins with possibly different hydrometeor phases. To consider this potential variability inherent to an RYups/DPRans estimate, we define an adjusted hydrometeor phase classification product aHPC as the volume fraction of liquid precipitation contained within a RYups pixel as

$$aHPC = L/(L + M + S) \qquad (2.1)$$

with L/S/M the number of DPR vertical bins, which contain only liquid/solid/mixed precipitation, respectively. Accordingly, with aHPC = 1 the RYups estimate contains only liquid precipitation (according to the DPR phase profile), and with aHPC = 0 no liquid precipitation is present in the DPR profile and thus also the RYups estimate.

We compare observations between 19 March 2014 and 03 January 2018 comprising a total of 2661 GPM overflights over the DWD radar composite area. The DWD radars have a minimum sensitivity of −32.5 dBZ (BARTELS et al., 2004), while the sensitivity of the DPR Ka-band radar is +12 dBZ (which corresponds to a minimum detectable rain rate of about 0.2 mm/h) and of the Ku-band +18 dBZ (which corresponds to a minimum detectable rain rate of about 0.5 mm/h; IGUCHI et al., 2017). The rain/no-rain threshold chosen in earlier comparison studies differ considerably. E.g. SPEIRS et al. (2017) took the higher one of the minimum detection thresholds from both data sources as the comparison threshold (Minimum Value). PETRACCA et al. (2018) used the pre-launch determined DPR threshold of 0.5 mm/h (IGUCHI et al., 2017) for their analysis (Prelaunch Nominal). WATTERS et al. (2018) determined the comparison threshold as the one, which maximizes the Heidke Skill Score (Maximum HSS) between both data sets (for details see WATTERS et al., 2018 and KIRSCHBAUM et al., 2012). In this study we apply all three methods, examine the differences, and select one threshold for the final comparison between DPRans and RYups (Section 3.1).

We exclude from our DPRans comparison data with DPR observations classified as Heavy Iced Precipitation (HIP). This GPM classification indicates high reflectivities (>35 GHz at Ku- and >30 GHz at Ka-band) caused by ice particles at heights around the −10°C isotherm above storms (IGUCHI et al., 2017). These reflectivities are often the results of non-Rayleigh scattering and are potentially affected by multi-scattering (BATTAGLIA et al., 2007; BATTAGLIA et al., 2010; IGUCHI et al., 2018). These processes might adversely affect precipitation estimates (BATTAGLIA et al., 2015).

2.4 Sources for discrepancies between DPRns and RYups

In this section, we highlight the potential problems, when comparing DPRns with RYups in order to motivate the new DPRans product. Figure 3 displays an example

of GPMs DPRns instantaneous rain rates (top left), the RY product (top right) upscaled to the DPR grid resolution (RYups) as described in the previous section, and a track-height cut (indicated with a thick black line in the upper left sub-figure) through the DPR rain rate product including the RYups product with its mean beam height and width. This example suggests a systematic rain rate disagreement between both data sets with RYups higher by 0.86 mm/h (compare color-coded circles with background color). The following conditions may lead to such differences (compare bottom part of Figure 3 and other Figs. noted):

- Spatial mismatch (position and extent) between the observed volumes contributing to the products; compare the vertical black lines assigned to every RYups circle with the height of the clutter-free bottom (continuous black line) for which the DPR product is representative.
- Precipitation estimates pertain to different phases (e.g. at 10.7° longitude where RYups refers to a level above and DPRns to a level below the melting layer).
- Impact of terrain; while the height of the DPRns estimate depends on local elevation, the height of the RYups estimate is given by the elevation-following scanning strategy.
- Errors in the determination of the CFB (see also WATTERS et al., 2018); e.g. at 9.5° longitude where the CFB misplacement above the melting layer leads to an extrapolation of rain rates estimated in the ice region down to the surface. Thus, when the bright band is below the CFB while RYups measuring below it, the latter will usually be larger.
- Ground-based radar observing volumes contributing to RYups increase with distance from the radar and might cover up to 18 (vertical) DPR layers (Figure 1, right) containing a set of different hydrometeor phases. This may lead to non-uniform phase beam-filling effects in the RYups product.
- RYups bins may be observed completely above the precipitating part of a cloud while its corresponding DPRns precipitation value is estimated in the liquid part close to the ground (e.g. between 10.5° and 11° longitude).
- DPRns observations are mostly below 1 km, but strongly depend on the local observation zenith angle (Figure 4, top-right) leading to differences of up to 3 km between the heights of the inner and outer parts of the swaths. This zenith dependency reduces the detection quality of low bright bands in the outer part of the swath, a problem also noted for TRMM (AWAKA et al., 2009). The ground-based measurements on the other hand vary between close to the ground to 5 km due to the terrain-following scanning (Figure 4).

2.5 Comparison statistics

We compare precipitation occurrences (yes/no) between DPRans and RYups, followed by a quantitative com-
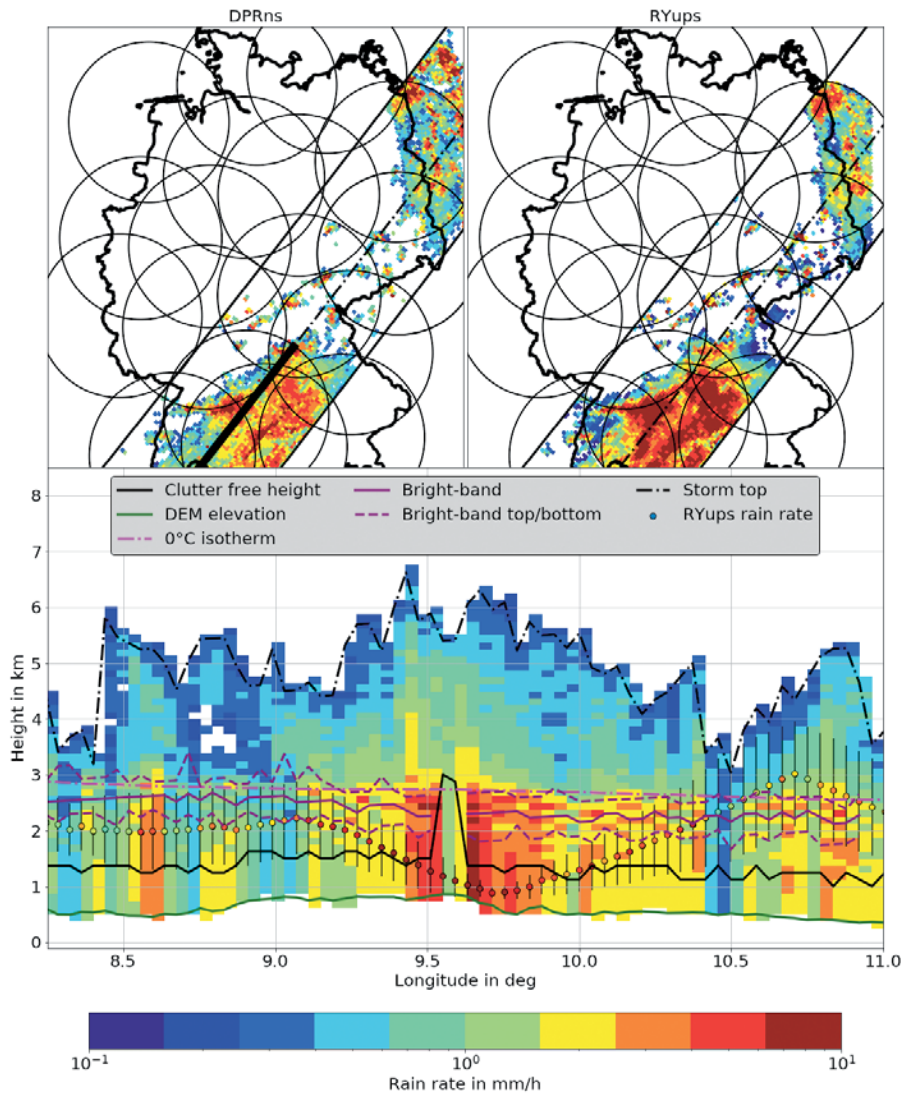
Figure 3: (Top left) DPRns from a GPM overpass on 2014–08-31 crossing Germany at 12:54 UTC and (top right) RYups observation upscaled to the DPRns grid. The thick black line indicates the position of the height-longitude cut through the GPM 3D precipitation field displayed at the bottom. The colors indicate the estimated precipitation rate in mm/h. (Bottom) The clutter-free height is shown as a black line. Other DPR parameters are noted in the legend. The circles are RYups observation heights colored according to the precipitation rate. The vertical bars represent the extent of the RYups beam widths for that particular profile.

parison for cases when both observation systems detect precipitation. The detection agreement is quantified via contingency tables with H (Hit) the number of cases when both RYups and DPRns/ans indicate precipitation, FT (False DPR, True RY) the number of cases when RYups detects precipitation but DPRns/ans not, and TF (True DPR, False RY) when DPRans detects precipitation while RYups does not. From the contingency table we calculate

$$CSI = \frac{H}{FT + H + TF} \qquad (2.2)$$

$$FAR = \frac{TF}{H + TF} \qquad (2.3)$$

$$IFAR = \frac{FT}{H + FT} \qquad (2.4)$$

with CSI the Critical Success Index, FAR the false alarm ratio, and IFAR the inverse false alarm ratio. CSI quantifies the degree of agreement from 0 (no agreement) to 1 (total agreement) following CHOKNGAMWONG and CHIU (2008). FAR and IFAR quantify the detection discrepancy, e.g. when FAR or IFAR is 0 there are no detection discrepancies. When FAR approaches 1, DPRans detects precipitation much more often than RYups, and vice versa when IFAR approaches 1.

The correspondence between the detected precipitation intensities of both observing systems is quantified via the mean difference (bias), the root mean square of the difference (RMSD), the unbiased RMSD (ubRMSD), and Pearson's correlation coefficient (r) via:

$$bias = \frac{1}{n} \sum_{i=1}^{n} (x_i - y_i), \qquad (2.5)$$
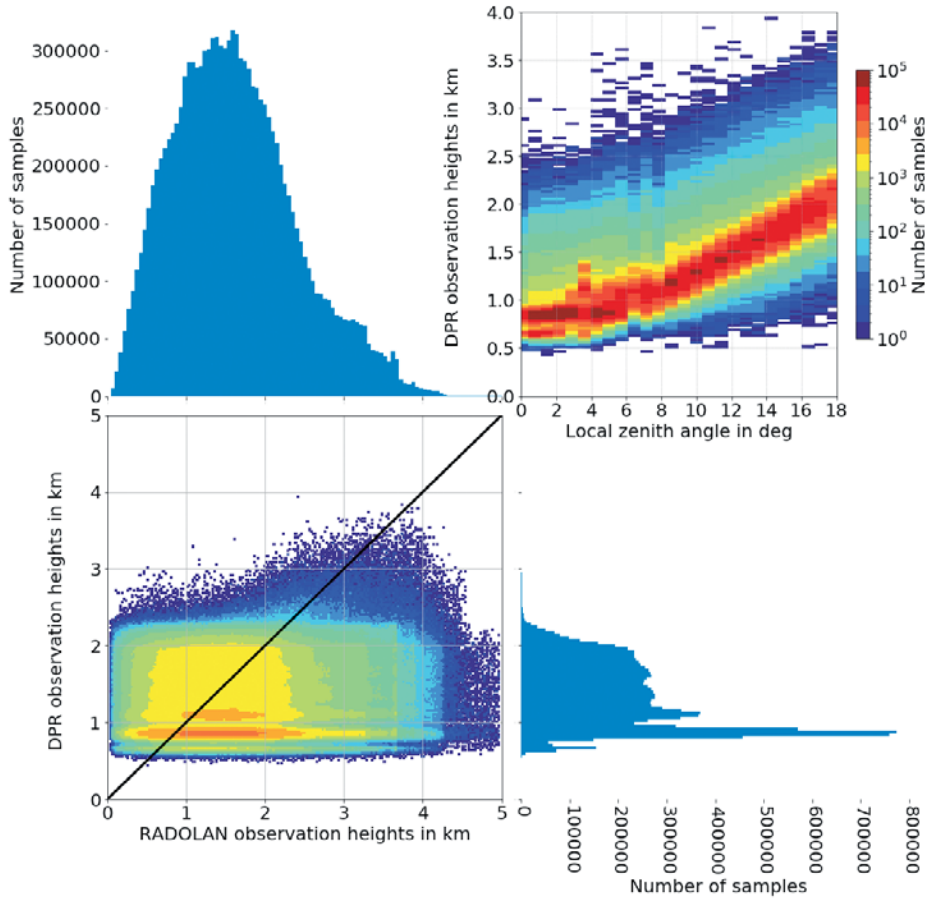
Figure 4: (Bottom left) 2D-histogram of three years of RYups observation heights versus the corresponding standard DPR near surface product (DPRns) observation heights with the marginal DPR (bottom right) and RYups observation height histograms (top left). The right top sub-figure shows for the same period the distribution of the heights of the DPRns product versus the local zenith angle.

$$RMSD = \sqrt{\frac{1}{n} \sum_{i=1}^{n} (x_i - y_i)^2}, \qquad (2.6)$$

$$ubRMSD = \sqrt{RMSD^2 - bias^2}, \qquad (2.7)$$

$$r = \frac{\sum_{i=1}^{n} (x_i - \bar{x})(y_i - \bar{y})}{\sqrt{\sum_{i=1}^{n} (x_i - \bar{x})^2 \sum_{i=1}^{n} (y_i - \bar{y})^2}} \qquad (2.8)$$

with x_i the DPRns/ans estimates, $\bar{x}$ their average, y_i the RYups rain rates, and $\bar{y}$ their average. A negative bias indicates that RYups estimates higher rain rates than DPRns/ans, and vice versa.

3 Results

3.1 DPRns against DPRans

Figure 5 compares RYups and DPRns/DPRans after applying the three rain/no-rain thresholds in Table 1 (indicated in bold). While WATTERS et al. (2018) got a rain/no-rain threshold of 0.38 mm/h for the maximum Heidke Skill Score (HSS) of 0.74, we find a threshold of 0.28/0.25 mm/h for a maximum HSS of 0.76/0.75 for DPRans/DPRns. Similar to SPEIRS et al.

(2017) we find the lowest non-zero rain value for DPRns around 0.02 mm/h because of the high sensitivity of the Ka-band in the inner swath and the more accurate dual-frequency retrieval algorithm. DPRans even leads to a threshold below 0.001 mm/h due to the column averaging. The pre-launch threshold omits a considerable amount of data in the analysis, a choice only recommended when data below the threshold are analyzed as in PETRACCA et al. (2018). The lowest RMSD and ubRMSD and the highest correlation are found when the Minimum Value threshold method is used (Figure 5, middle row). With the pre-launch threshold, RMSD and ubRMSD are highest and correlations are lowest (Figure 5, bottom row). In general, compared to DPRns the DPRans estimates are closer to the RYups estimates regardless of the threshold used, however at the expense of a slightly larger bias. In the following, we use the threshold resulting from the Minimum Value method, i.a. 0.02 mm/h.

In order to examine the effects of the mismatch of measurement height and beam width when comparing DPRns with RYups, we calculated and compared the correlation r, ubRMSD and bias (DPRns/ans–RYups) as a function of the height difference between RYups and DPRns (Figure 6). As expected by matching the
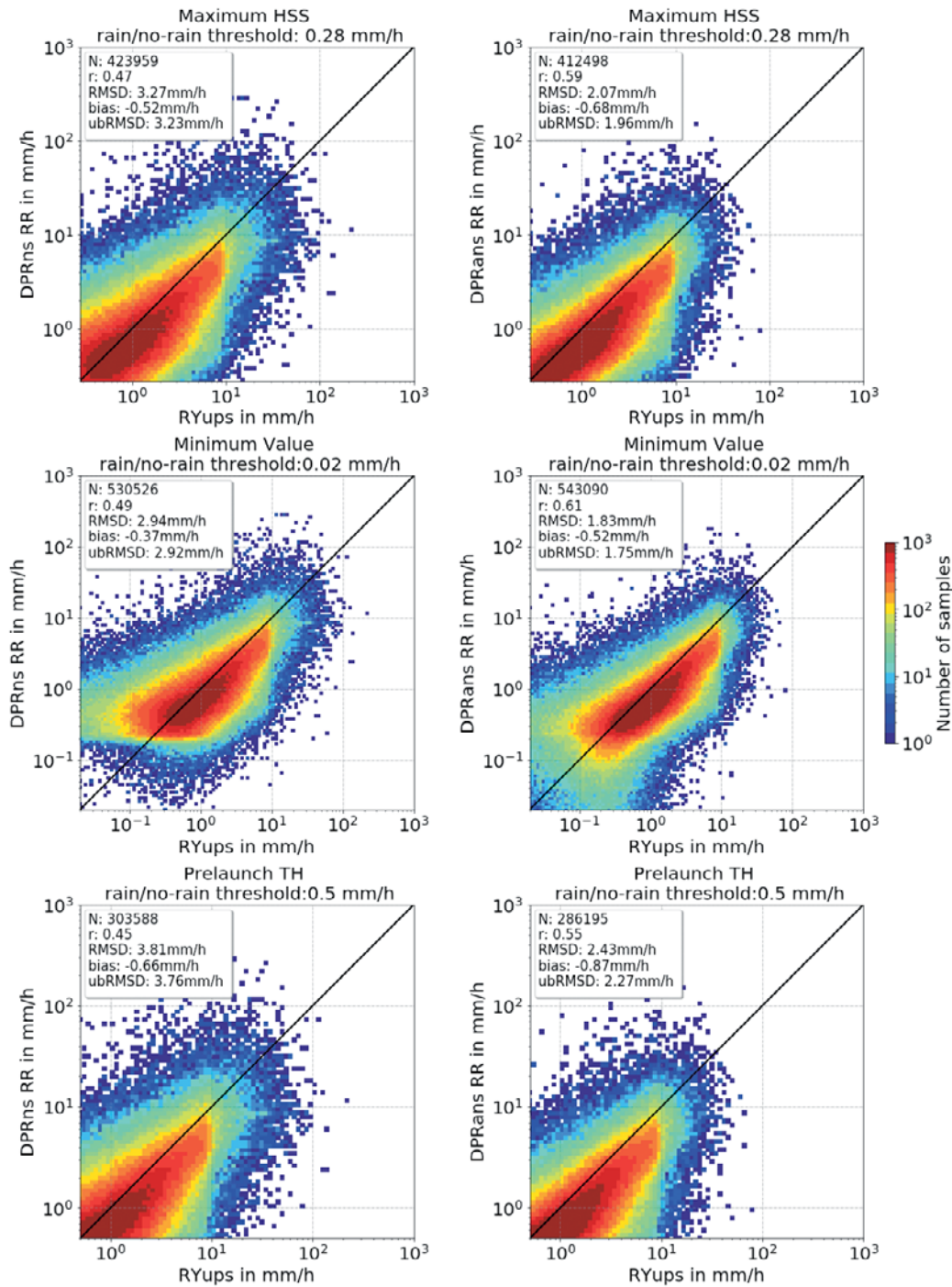
Figure 5: Scatterplots of RYups versus standard (DPRns, left) and adjusted near surface DPR rain rates (DPRans, right) after applying thresholds derived via HSS (top row), Minimum Value (middle row), and Prelaunch nominal (bottom row). Colors indicate the number of observations and the black line the 1:1 relationship. Total number of observations N, correlation coefficient r, root mean square of the difference RMSD, unbiased root mean square of the difference ubRMSD, and bias are given in the legend box. The rain/no-rain threshold value is indicated in the title.

Table 1: Rain/ no-rain thresholds calculated for the comparisons of RYups with standard (DPRns) and adjusted DPR rain rates (DPRans) determined with three methods used in other studies (see Section 2.4). Bold values indicate the thresholds later used for the comparison in Figure 5.

Method	Reference and their result [mm/h]	DPRns [mm/h]	DPRans [mm/h]
Maximum HSS	0.38 (WATTERS et al., 2018)	0.25	**0.28**
Minimum Value	0.02 (SPEIRS et al., 2017)	**0.02**	<0.001
Prelaunch Nominal	0.50 (PETRACCA et al., 2018)	**0.50**	**0.50**
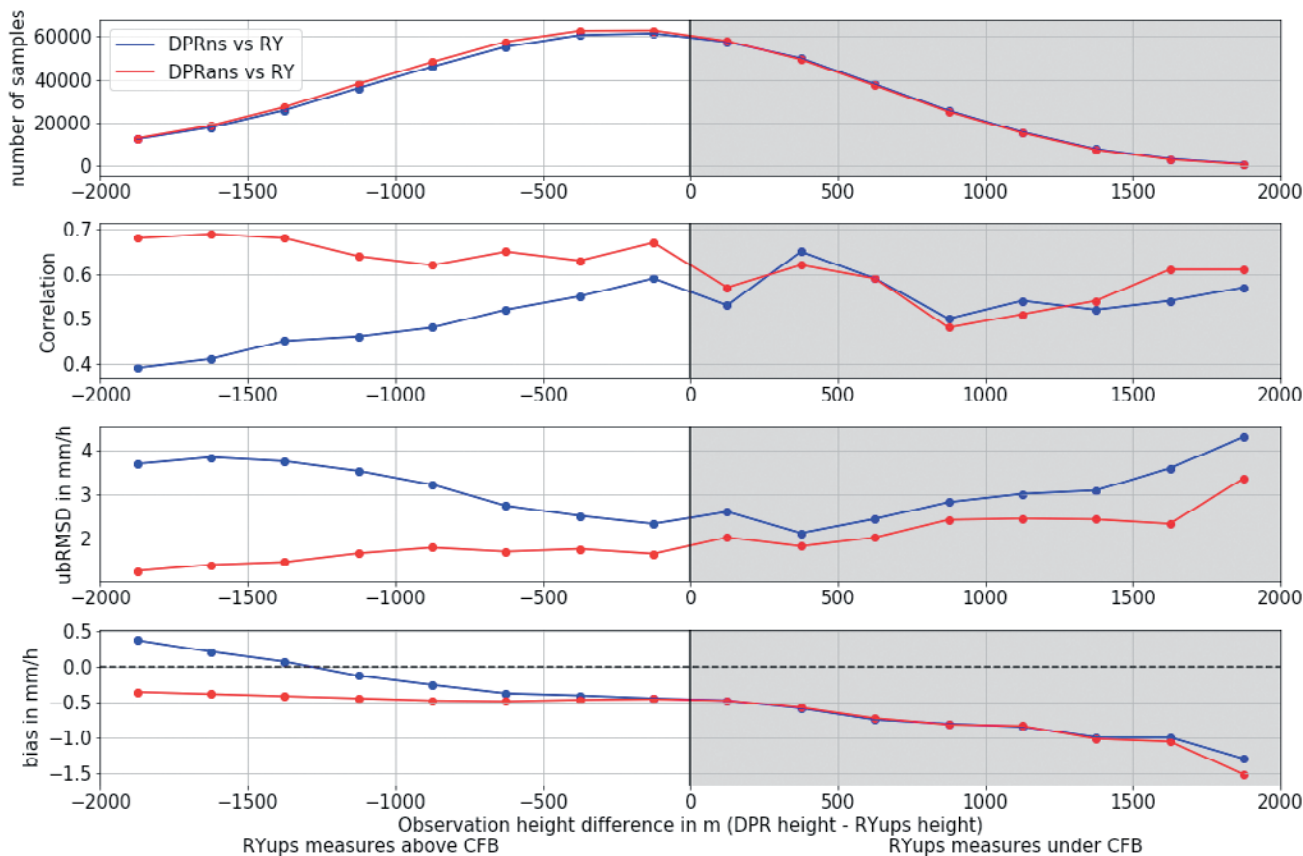
Figure 6: Number of samples (top), correlation (second), unbiased RMSD (third) and bias (bottom) of RYups versus DPRns (blue) and DPRans (red) as a function of the difference between the DPRns observation height and the RYups observation height. The shaded area indicates the region where the measurements from the ground-based radars are below the CFB of the space borne radar.

observation heights in DPRans the statistics significantly improve with increasing height differences for RYups pixels above the CFB (left white area), but minor or close to no improvements for RYups pixels observed below the CFB (right grey area). For the latter, DPR provides measured rain rates from the top of the cloud to CFB; below the CFB the data results from extrapolating the rain rates from the CFB to the ground level which only leads to minor changes of rain rates below the CFB and in turn only minimal improvements through the adjustments in DPRans below or near the CFB. Overall, the ubRMSD, r and bias for DPRans (red lines on the white left side of Figure 6) confirm, that we significantly reduced the effects of the observation height and beam width mismatch with DPRans.

When RYups is observed at high altitudes (i.e. at far range from the radar) while DPRns is observed close to the surface, DPRns is on average larger than RYups (blue line in bottom left Figure 6) in spite of the overall negative bias of DPRns (Figure 5). This is expected, because RYups might have been observed in the upper part of a cloud where cloud droplets or ice particles give rise to lower reflectivities as the rain below observed by DPRns (see also WATTERS et al., 2018). When we compare pixel-by-pixel the hydrometeor phase classification between DPRns and DPRans, 41 % of the pixels have

different phases (Figure 7). E.g. 27 % of the mixed phase pixels in DPRans are liquid and 8 % solid in DPRns.

3.2 Comparison between DPRans and RYups precipitation rates

Due to the large differences in observations heights and accordingly also hydrometeor phases between DPRns and RYups, we confine the precipitation rate comparisons to DPRans and RYups. We start with a separation between stratiform and convective cases. The impact of orography, hydrometeor phases and season is analyzed only for stratiform events, which allow for a robust identification of the bright band and thus a sufficient distinction between hydrometeor phases.

According to the GPM DPR precipitation regime classification into convective, stratiform and other, stratiform events are almost ten times more frequent than convective events (Figure 8). In stratiform conditions, DPRans (when compared to RYups) overestimates the occurrence of precipitation below 1 mm/h, underestimates between 1 mm/h and 10 mm/h, and again overestimates the occurrence of precipitation above 10 mm/h. Convective cases show similar differences, however at different spans of rain rates. In general, DPRans and RYups correlate stronger and have lower RMSD and
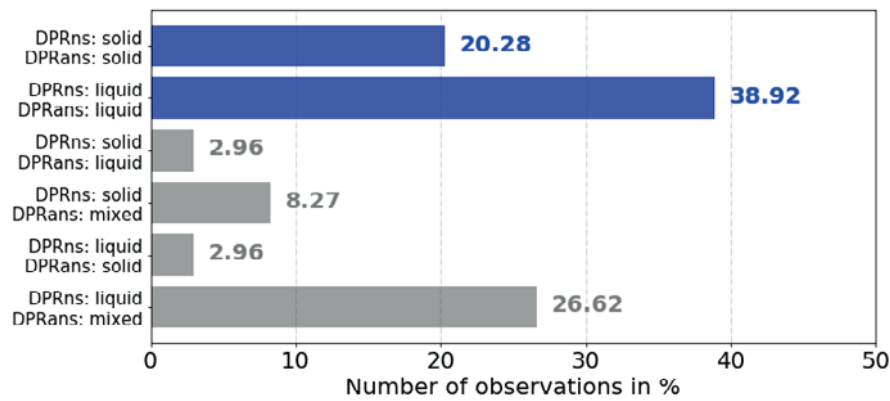
Figure 7: Bar plot showing the consistency of the hydrometeor phase classification between DPRns and DPRans. The blue bars show the number of measurements where both phase classification matches, while the grey bars show the number of mismatches.
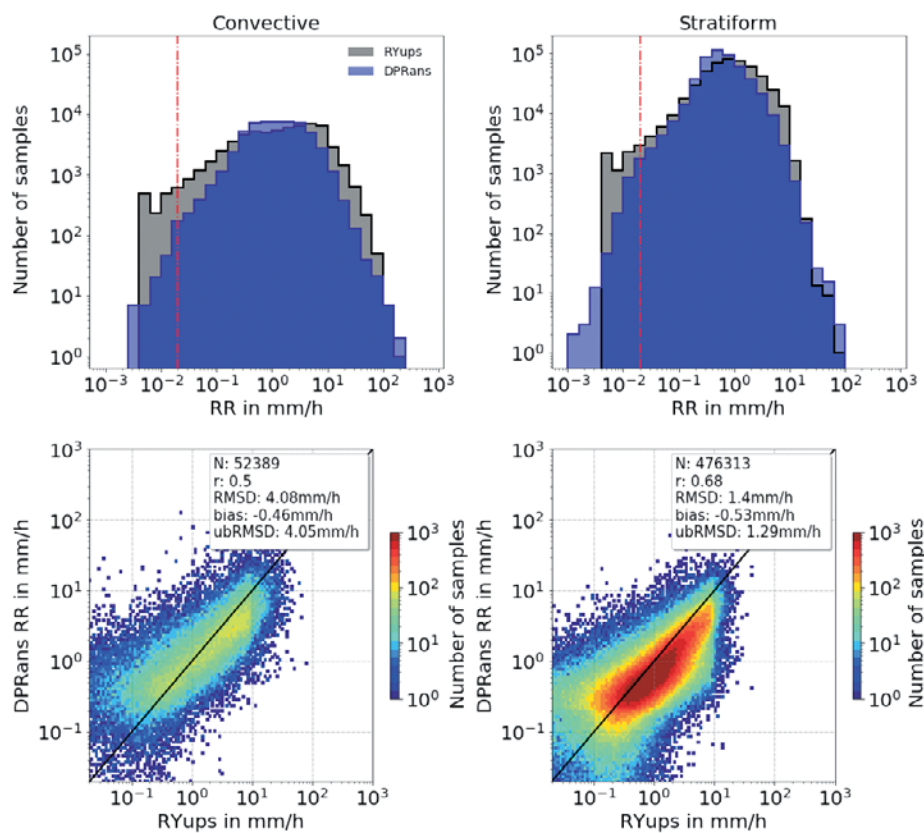

Figure 8: Distribution of precipitation rates for the RYups product and the DPRans product for convective (top left) and stratiform cases (top right). The vertical dashed-dotted lines indicate the threshold rain intensity of 0.02 mm/h. Scatterplot of RYups versus DPRans precipitation rates for the same cases (bottom). The black line is the 1:1 line.

ubRMSD for stratiform than for convective precipitation.

In stratiform precipitation DPRans overall underestimates precipitation compared to RYups for all precipitation phases (Figure 9). The lower bias for solid precipitation is most probably caused by the much smaller precipitation range which only extends up to 10 mm/h. For the same reason RMSD and ubRMSD are higher in pure liquid compared to solid and practically equal to mixed-phase precipitation. For the latter, DPRans precipitation generally underestimates (compared to RYups) most probably because the bright band produces a more intense reflectivity signal at lower frequency bands (C-band) as compared to DPR's Ku and Ka-band. (KOLLIAS and ALBRECHT, 2005). Thus RYups overestimates precipitation rates because the applied z-R-relations are valid only for liquid precipitation. See also the systematic deviations for solid precipitation.

We made the comparisons separately for seasons, but present for simplicity only the results for summer and winter as spatial distributions of the correspondence measures on a 20 km x 20 km grid (Figure 10). A reliable
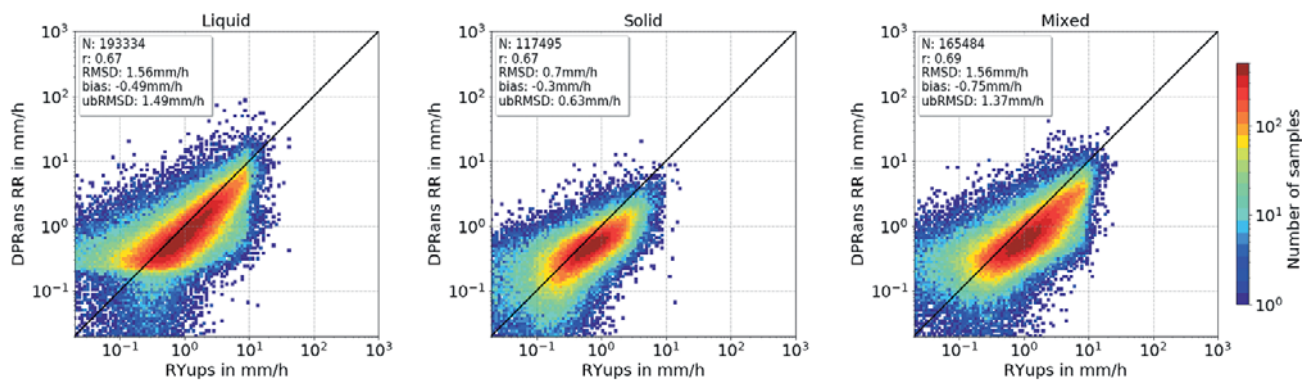
Figure 9: Scatterplot between RYups and DPRans separated by precipitation phase (aHPC) into pure liquid phase (left), pure solid phase (center), and mixed phase (right). The black line is the 1:1 relation and the color indicates the number of samples.
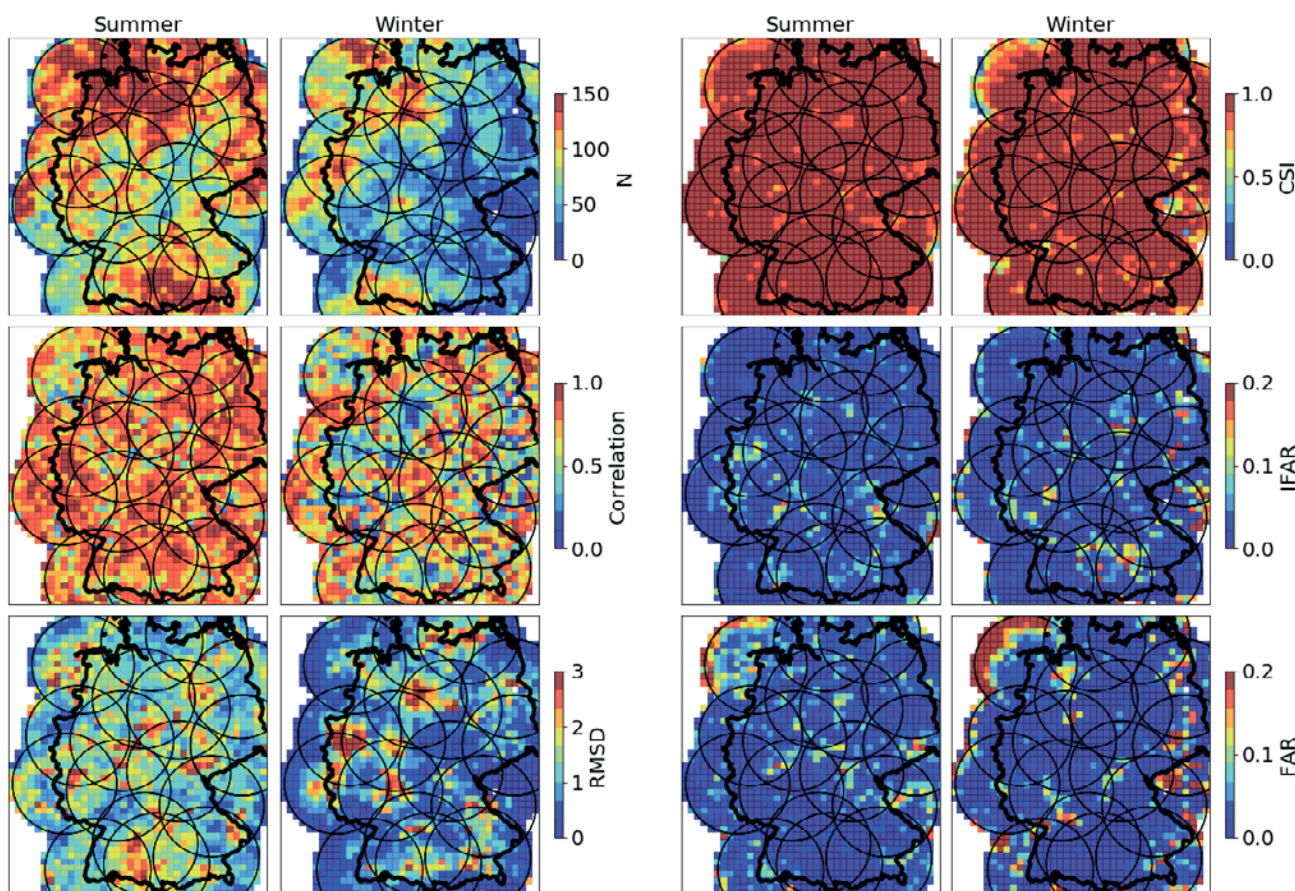

Figure 10: Number of observations, correlation and RMSD of DPRans and RYups for summer (first column) and for winter (second column). Seasonal CSI, FAR and IFAR of DPRans and RY for summer (third column) and winter (fourth columns). All observations are binned on a 20 km × 20 km grid. Rain/no-rain threshold = 0.02 mm/h.

detection of the bright band height (again we restrict the analysis to stratiform precipitation) is key for a high-quality precipitation rate retrieval, since it is used to assign precipitation types to the DPR. During winter the height of the bright band is typically low and in some cases below or near to the DPR's CFB height, which leads to a poor phase classification. In summer, the bright band is usually much higher than the CFB and can

be more easily detected and allows for a more accurate phase classification and thus better precipitation rate determination.

Accordingly, the correlations between both datasets are high and quite homogeneous in summer. In winter, higher correlations occur mostly in areas of overlapping ground-based radar scans where the observation altitude is quite high and mostly above the CFB. The
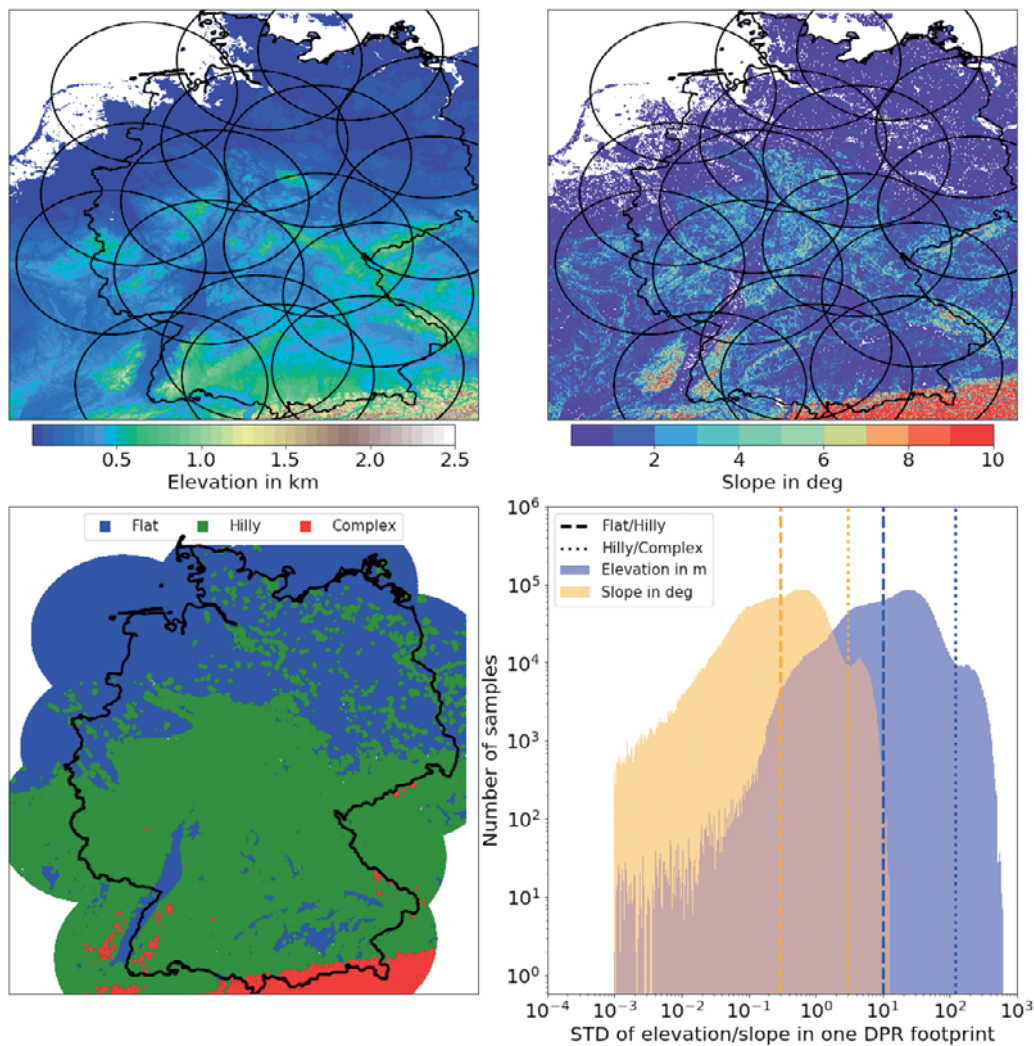
Figure 11: Elevation above sea level in km of the orography in the RADOLAN region (top left). The slope in degree calculated from the DEM (GTOPO30, 1997) model elevations (top right). Histograms of the elevation standard deviation in m and slope standard deviation in degree per DPR footprint with defined thresholds for the classification of terrain type (bottom right). The separation with slope (orange)/elevation (blue) of flat/hilly is indicated with the dashed lines and for hilly/complex is indicated with the dotted lines. Classification of flat, hilly and complex terrain (bottom left).

overall correlation/RMSD in summer is 0.7/1.59 mm/h and in winter 0.55/1.29 mm/h (not shown). In winter the RMSD shows particularly high values together with low correlation in the vicinity of some radar locations in flat terrain, i.e. in areas in which ground-radars usually measure below the CFB. In terms of skill scores, the CSI shows similar detection performance in summer and winter; also the false alarm ratio (FAR) and the inverse false alarm (IFAR) are similar in both seasons. The overall CSI for winter and summer is 0.94 and FAR/IFAR are for summer 0.03/0.02 and 0.04/0.02 (not shown). A particularly high FAR (DPRans detects more often precipitation occurrence than RYups) is found in the northwestern area mainly because is monitored by the Emden aged single-pol radar, hinting at large detection inaccuracies in that area probably due to uncorrected clutter produced by offshore wind farms and marine traffic besides a less than optimal radar.

Not only ground radars are influenced by terrain complexity via beam blockage or overshooting; also satellite-based precipitation estimates suffer from orographic effects. Complex surface geometry leads to a high spatial in-homogeneity of the surface cross sections that has an impact on DPRs attenuation correction (D'ADDERIO et al., 2018; MENEGHINI et al., 2015) and an increasing in the height of the CFB (IGUCHI et al., 2017; KUBOTA et al., 2016; KULIE and BENNARTZ, 2009). Therefore, the effects of land types and surface complexities are examined. Over Germany only two lakes are identified in the DPR data as inland water, which we will not consider here. All other lakes, rivers, and coastal areas are classified as coastal. In order to quantify RYups and DPRans data comparisons according to topography we use the standard deviation of terrain height (Figure 11, top left) and the standard deviation of terrain slope (Figure 11, top right) within each

Table 2: Definition for terrain classification into flat, hilly, complex and other with standard deviation of slope in degree per DPR footprint, standard deviation of elevation in meter per DPR footprint and percentage of data.

	Class 1: Flat	Class 2: Hilly	Class 3: Complex	Undefined
STD(Slope)	<0.3°	0.3°–3°	>3°	–
STD(Elevation)	<10 m	10 m–120 m	>120 m	–
Percentage of data	41 %	47 %	3 %	9 %

Table 3: Detection capability CSI, IFAR and FAR and estimation agreement correlation, bias, and RMSD for different land surface types (left) and different terrain classes (right). Note that RMSD and bias in mm/h.

	Land surface type			Terrain classes		
	Coast	Land	Ocean	Flat	Hilly	Complex
r	0.70	0.69	0.63	0.66	0.68	0.65
bias	−0.46	−0.56	−0.31	−0.50	−0.53	−0.35
RMSD	1.34	1.41	1.35	1.39	1.40	1.27
CSI	0.95	0.96	0.89	0.94	0.95	0.91
IFAR	0.02	0.02	0.02	0.02	0.02	0.02
FAR	0.04	0.03	0.09	0.04	0.03	0.04

DPR footprint. Their distributions exhibit three main regimes (Figure 11, bottom right), which we classify as class 1 (flat), class 2 (hilly) and class 3 (complex) regions (Figure 11, bottom left, and Table 2). Mixed surface types are not considered in the comparisons.

Note that we only compare the detection of the two observing systems and if they detect the same without using one of these as a reference. The detection performance (CSI) is mostly high along the coast and over land but low over the ocean. The highest FAR is over ocean followed by coast and land. However, FAR is always higher than the IFAR (Table 3, left), thus DPRans detects more often precipitation than RYups. Especially over the ocean ground-based radar observations suffer from clutter by ships and offshore wind farms, which cannot be efficiently removed since polarimetric methods are not yet used by the RADOLAN composite processor. The lowest absolute bias appears over the oceanic areas located at the northern borders of the composites where observations are taken at far ranges and thus more often in the ice phase.

The terrain following scans of the ground-based radars have a higher elevation angle over class 3 (complex) areas whereby mainly measurements from solid precipitation are compared. This causes, as shown in figure 9, a lower absolute bias and low RMSD. In general, correlations are lower over class 3 (complex) where the CFB increases because of the terrain complexity, but also in class 1 (flat) areas where the ground radar measures below CFB. Table 3 shows that CSI suggests there are no major differences in detection capabilities. Over class 3 (complex) the CSI shows the lowest value. These can be a consequence of the fact that CFB is higher over mountain regions.

4 Summary and discussion

We compared composite precipitation estimates (RY) computed from the DWDs C-band radar network with retrievals from the DPR instrument on the GPM core satellite and in particular. Direct comparisons of the standard DPR near surface product (DPRns) with the RY product upscaled to the DPR footprint (RYups) suffer from spatial mismatches of the sampling volumes. Thus, we used the DPR columnar precipitation estimates to create a new near-surface DPR product (DPRans), which optimizes the overlap in height and beam width with the ground-based radar estimate. This adaptation requires also an adjustment of the GPM hydrometeor phase attribution (aHPC).

For a first comparison between RYups and DPRns and the new DPRans product, we used three rain/no rain threshold determination methods. The maximum HSS (WATTERS et al., 2018) yielded a threshold of 0.38 mm/h, the Minimum Value (SPEIRS et al., 2017) 0.02 mm/h, and the prelaunch Nominal (PETRACCA et al., 2018) assigned to 0.5 mm/h. We use for our study the threshold of 0.02 mm/h. The adjustment of the DPR measurements to the height and width of the ground-based radar composite (DPRans) enhanced the correlation with RYups from 0.49 to 0.61, reduced the RMSD from 2.94 mm/h to 1.83 mm/h, but slightly increased the bias relative to RYups from −0.37 to −0.52 mm/h.

The lower rain rates from RYups compared to DPRns in regions where the ground-based radar observes at higher altitudes (outer radar region) are caused by the often solid precipitation seen by the latter (low reflectivity) while DPSns is observed near the surface mostly in the liquid or mixed phase (Figure 6, blue curve; WATTERS et al. (2018), Figure 8). DPRans solves this mismatching and does not show this bias. The hydrometeor phase classification product adjusted to DPRans (aHPC) takes non-uniform hydrometeor-phase beam filling into account and thus avoids incoherent phase attributions between both products.

The correlation is higher and the RMSD lower between RYups and DPRans in stratiform compared to convective precipitation. The separation into solid, mixed and liquid rain estimates (only analyzed for stratiform precipitation) shows the best agreement between both data sets for liquid precipitation, which recommends to a phase separated z-R relationship within the RADOLAN procedure. The highest correlation and lowest RMSD between RYups and DPRans are found in summer. Larger deviations are found in winter near the ground-based radar locations when the melting layer is

close to the ground and below the CFB of the DPR. There is no seasonal dependence in the mutual precipitation detection agreement between RYups and DPRans unlike other studies using the standard DPRns, reported by Speirs et al. (2017) and Petracca et al. (2018). Our study concludes that those seasonal dependencies could have been caused by spatial mismatching. Increased FAR values in the northwest of the RADOLAN composite and higher IFAR values near the radar sites probably arise from a non-polarimetric clutter filter in RADOLAN procedure.

In terms of terrain effects the highest detection agreement is over hilly and flat terrain where the effects of the ground clutter do not have such a large impact on both space-borne and ground-based measurements. The correlations, absolute bias and RMSD between both data sets are lowest over class 3 (complex) and highest over class 1 and class 2 (flat and hilly). Speirs et al. (2017) reported lowest absolute bias and RMSD in flat terrain. Apart from the fact that the terrain classification methods are different, it can be assumed that our definition of class 1 (flat) and class 3 (complex) mostly corresponds to the classification of flat and complex terrain by Speirs et al. (2017) which is only determined by standard deviation of elevation. We suggest that the main source of the difference is due to the adjusted DPRans that we are using.

We propose, given the composite configuration of the DWD's radars, that our new product DPRans provides the best possible agreement between space-borne and ground-based precipitation estimates. We suggest that a direct comparison using reflectivities instead of rain retrievals is the next step, thus unknown effects introduced by assuming certain z-R-relationship can be discarded. The comparison can be extended to the attenuation corrections and the validity of the different z-R-relationships used in RADOLAN and the DPR processing. Furthermore, a temporally extended comparison would allow an evaluation of derived precipitation estimates with polarimetric information (POLARA, applied for RY from October 2017; Deutscher Wetterdienst, 2020). Comparisons with homogenized data like RADKLIM (Winterrath et al., 2017) could also be used to examine the uncertainties introduced by new reprocessing methods hence its rain rate estimates as shown in this contribution. All studies so far suggest, that DPR yields significantly lower rain rates compared to ground-based radars (Speirs et al., 2017; Petracca et al., 2018; Watters et al., 2018) while studies comparing reflectivities show lower reflectivities of ground-based radars (Crisologo et al., 2018; Keem et al., 2019; Biswasand Chandrasekar, 2018). The approach presented by this study paves the way to solve this contradiction, since circumventing the spatial mismatch leads to a dataset suitable for comparisons either for rain rates or reflectivity. This method has the potential to be applied to different composites outside the RADOLAN region. In this case, an adaptation to the specific geometry of the selected radar network, as described in this contribution, is required.

References

Auerswald, K., F.K. Fischer, T. Winterrath, R. Brandhuber, 2019: Rain erosivity map for Germany derived from contiguous radar rain data. – Hydrol. Earth Sys. Sci. **23**, 1819–1832, DOI: 10.5194/hess-23-1819-2019.

Awaka, J., T. Iguchi, H. Kumagai, K. Okamoto, 1997: Rain type classification algorithm for TRMM precipitation radar. – In: IGARSS'97. 1997 IEEE International Geoscience and Remote Sensing Symposium Proceedings. Remote Sensing – A Scientific Vision for Sustainable Development, volume 4, 1633–1635 vol. 4. DOI: 10.1109/IGARSS.1997.608993.

Awaka, J., T. Iguchi, K. Okamoto, 2009: TRMM PR Standard Algorithm 2A23 and its Performance on Bright Band Detection. – J. Meteor. Soc. of Japan. Ser. II **87A**, 31–52, DOI: 10.2151/jmsj.87A.31.

Awaka, J., M. Le, V. Chandrasekar, N. Yoshida, T. Higashiuwatoko, T. Kubota, T. Iguchi, 2016: Rain Type Classification Algorithm Module for GPM Dual-Frequency Precipitation Radar. – J. Atmos. Ocean. Technol. **33**, 1887–1898, DOI: 10.1175/JTECH-D-16-0016.1.

Barros, A., W. Petersen, M. Schwaller, R. Cifelli, K. Mahoney, C. Peters-Liddard, M. Shepherd, S. Nesbitt, G. Wolff, D. Heymsfield, D. Starr, 2014: NASA GPM-Ground Validation: Integrated Precipitation and Hydrology Experiment 2014 Science Plan. – EPL/Duke University, 64 pp., DOI: 10.7924/G8CC0XMR.

Bartels, H., E. Weigl, T. Reich, P. Lang, A. Wagner, O. Kohler, N. Gerlach, 2004: Projekt RADOLAN Routineverfahren zur Online-Aneichung der Radarniederschlagsdaten mit Hilfe von automatischen Bodenniederschlagsstationen (Ombrometer). – https://www.dwd.de/DE/leistungen/radolan/radolan_info/abschlussbericht_pdf.pdf?__blob=publicationFile&v=2.

Battaglia, A., M.O. Ajewole, C. Simmer, 2007: Evaluation of radar multiple scattering effects in Cloudsat configuration. – Atmos. Chem. Phys. **7**, 1719–1730, DOI: 10.5194/acp-7-1719-2007.

Battaglia, A., S. Tanelli, S. Kobayashi, D. Zrnic, R.J. Hogan, C. Simmer, 2010: Multiple-scattering in radar systems: A review. – J. Quantitative Spectroscopy Radiative Transfer **111**, 917–947, DOI: 10.1016/j.jqsrt.2009.11.024.

Battaglia, A., S. Tanelli, K. Mroz, F. Tridon, 2015: Multiple scattering in observations of the GPM dual-frequency precipitation radar: Evidence and impact on retrievals. – J. Geophs. Res. Atmos. **120**, 4090–4101, DOI: 10.1002/2014JD022866.

BISWAS, S.K., V. CHANDRASEKAR, 2018: Cross-Validation of Observations between the GPM Dual-Frequency Precipitation Radar and Ground Based Dual-Polarization Radars – Remote Sens. **10**, 1733, DOI: 10.3390/rs10111773.

CANNON, F., F.M. RALPH, A.M. WILSON, D.P. LETTENMAIER, 2017: GPM Satellite Radar Measurements of Precipitation and Freezing Level in Atmospheric Rivers: Comparison With Ground-Based Radars and Reanalyses. – J. Geophs. Res. Atmos. **122**, 12,747–12,764, DOI: 10.1002/2017JD027355.

CHEN, H., V. CHANDRASEKAR, R. BECHINI, 2017: An Improved Dual-Polarization Radar Rainfall Algorithm (DROPS2.0): Application in NASA IFloodS Field Campaign. – J. Hydrometeorol. **18**, 917–937, DOI: 10.1175/JHM-D-16-0124.1.

CHOKNGAMWONG, R., L.S. CHIU, 2008: Thailand Daily Rainfall and Comparison with TRMM Products. – J. Hydrometeorol. **9**, 256–266, DOI: 10.1175/2007JHM876.1.

CONRICK, R., C.F. MASS, 2019: Evaluating Simulated Microphysics during OLYMPEX Using GPM Satellite Observations. – J. Atmos. Sci. **76**, 1093–1105, DOI: 10.1175/JAS-D-18-0271.1.

CRISOLOGO, I., R.A. WARREN, K. MÜHLBAUER, M. HEISTERMANN, 2018: Enhancing the consistency of spaceborne and ground-based radar comparisons by using beam blockage fraction as a quality filter – Atmos. Meas. Tech. **11**, 5223–5236, DOI: 10.5194/amt-11-5223-2018.

DEO, A., S.J. MUNCHAK, K.J.E. WALSH, 2018: Cross Validation of Rainfall Characteristics Estimated from the TRMM PR, a Combined PR-TMI Algorithm, and a C-POL Ground Radar during the Passage of Tropical Cyclone and Nontropical Cyclone Events over Darwin, Australia. – J. Atmos. Ocean. Technol. **35**, 2339–2358, DOI: 10.1175/JTECH-D-18-0065.1.

DEUTSCHER WETTERDIENST, 2020: Informationen über Änderungen des operationellen RADOLAN-Betriebs. – https://www.dwd.de/DE/leistungen/radolan/radolan_info/radolan_informationen.html (Accessed: 2020.05.).

D'ADDERIO, L.P., G. VULPIANI, F. PORCÙ, A. TOKAY, R. MENEGHINI, 2018: Comparison of GPM Core Observatory and Ground-Based Radar Retrieval of Mass-Weighted Mean Raindrop Diameter at Midlatitude. – J. Hydrometeorol. **19**, 1583–1598, DOI: 10.1175/JHM-D-18-0002.1.

FISCHER, F., J. HAUCK, R. BRANDHUBER, E. WEIGL, H. MAIER, K. AUERSWALD, 2016: Spatio-temporal variability of erosivity estimated from highly resolved and adjusted radar rain data (RADOLAN) – Agricult. Forest Meteor. **223**, 72–80, DOI: 10.1016/j.agrformet.2016.03.024.

FURUKAWA, K., M. KOJIMA, T. MIURA, Y. HYAKUSOKU, H. KAI, T. ISHIKIRI, T. IGUCHI, H. HANADO, K. NAKAGAWA, M. OKUMURA, 2013: Satellite system test status of The Dual-Frequency Precipitation Radar on the global precipitation measurement core spacecraft. – In: 2013 IEEE International Geoscience and Remote Sensing Symposium – IGARSS, 1143–1146. DOI: 10.1109/IGARSS.2013.6721367.

GRECU, M., W.S. OLSON, S.J. MUNCHAK, S. RINGERUD, L. LIAO, Z. HADDAD, B.L. KELLEY, S.F. MCLAUGHLIN, 2016: The GPM Combined Algorithm. – J. Atmos. Ocean. Technol. **33**, 2225–2245, DOI: 10.1175/JTECH-D-16-0019.1.

GTOPO30, 1997: Research Data Archive at the National Center for Atmospheric Research, Computational and Information Systems Laboratory, USGS 30. – ARC-second Global Elevation Data, GTOPO30, DOI: 10.5065/A1Z4-EE71.

HEISTERMANN, M., J.S.T. PFAFF, 2013: Technical Note: An open source library for processing weather radar data (wradlib). – Hydrol. Earth Syst. Sci. **17**, 863–871, DOI: 10.5194/hess-17-863-2013.

HOU, A.Y., R.K. KAKAR, S. NEECK, A.A. AZARBARZIN, C.D. KUMMEROW, M. KOJIMA, R. OKI, K. NAKAMURA, T. IGUCHI, 2014: The Global Precipitation Measurement Mission. – Bull. Amer. Meteor. Soc. **95**, 701–722, DOI: 10.1175/BAMS-D-13-00164.1.

HOUZE, R., L. MCMURDIE, W. PETERSEN, M. SCHALLWER, 2015: OLYMPEX ground validation experiment field operations plan (version 3). – Tech. Rep., University of Washington.

HUFFMAN, G., D.T. BOLVIN, D. BRAITHWAITE, K. HSU, R. JOYCE, C. KIDD, E.J. NELKIN, P. XIE, 2015: NASA Global Precipitation Mea-surement Integrated Multi-satellitE Retrievals for GPM (IMERG). – Algorithm Theoretical Basis Doc., version 4.5.

IGUCHI, T., R. MENEGHINI, 2019: GPM DPR Precipitation Profile L2A 1.5 hours 5 km V06. – Greenbelt, MD, Goddard Earth Sciences Data and Information Services Center (GES DISC) (Accessed: 2019.10.), DOI: 10.5067/GPM/DPR/GPM/2A/05.

IGUCHI, T., T. KOZU, R. MENEGHINI, J. AWAKA, K. OKAMOTO, 2000: Rain-Profiling Algorithm for the TRMM Precipitation Radar. – J. Appl. Meteor. **39**, 2038–2052, DOI: 10.1175/1520-0450(2001)040<2038:RPAFTT>2.0.CO;2.

IGUCHI, T., S. SETO, R. MENEGHINI, N. YOSHIDA, J. AWAKA, M. LE, V. CHANDRASEKAR, T. KUBOTA, 2017: GPM/DPR Level-2 Algorithm Theoretical Basis Document. – https://www.eorc.jaxa.jp/GPM/doc/algorithm/ATBD_DPR_201811_with_Appendix3b.pdf.

IGUCHI, T., N. KAWAMOTO, R. OKI, 2018: Detection of Intense Ice Precipitation with GPM/DPR. – J. Atmos. Ocean. Technol. **35**, 491–502, DOI: 10.1175/JTECH-D-17-0120.1.

JUNGHÄNEL, T., C. BRENDEL, T. WINTERRATH, A. WALTER, 2016: Towards a radar- and observation-based hail climatology for Germany – Meteorol. Z. **25**, 435–445, DOI: 10.1127/metz/2016/0734.

KEEM, M., B.C. SEO, W.F. KRAJEWSKI, K.R. MORRIS, 2019: Inter-comparison of reflectivity measurements between GPM DPR and NEXRAD radars – Atmos. Res. **226**, 49–65, DOI: 10.1016/j.atmosres.2019.04.010.

KIM, J.H., M.L. OU, J.D. PARK, K.R. MORRIS, M.R. SCHWALLER, D.B. WOLFF, 2014: Global Precipitation Measurement (GPM) Ground Validation (GV) Prototype in the Korean Peninsula. – J. Atmos. Ocean. Technol. **31**, 1902–1921, DOI: 10.1175/JTECH-D-13-00193.1.

KIRSCHBAUM, D., R. ADLER, D. ADLER, C. PETERS-LIDARD, G. HUFFMAN, 2012: Global Distribution of Extreme Precipitation and High-Impact Landslides in 2010 Relative to Previous Years. – J. Hydrometeor. **13**, 1536–1551, DOI: 10.1175/JHM-D-12-02.1.

KOLLIAS, P., B. ALBRECHT, 2005: Why the melting layer radar reflectivity is not bright at 94 GHz. – Geophys. Res. Lett. **32**, published online, DOI: 10.1029/2005GL024074.

KUBOTA, T., T. IGUCHI, M. KOJIMA, L. LIAO, T. MASAKI, H. HANADO, R. MENEGHINI, R. OKI, 2016: A Statistical Method for Reducing Sidelobe Clutter for the Ku-Band Precipitation Radar on board the GPM Core Observatory. – J. Atmos. Ocean. Technol. **33**, 1413–1428, DOI: 10.1175/JTECH-D-15-0202.1.

KULIE, M.S., R. BENNARTZ, 2009: Utilizing Spaceborne Radars to Retrieve Dry Snowfall. – J. Appl. Meteor. Climatol. **48**, 2564–2580, DOI: 10.1175/2009JAMC2193.1.

KUMMEROW, C.D., D.L. RANDEL, M. KULIE, N.Y. WANG, R. FERRARO, S. JOSEPH MUNCHAK, V. PETKOVIC, 2015: The Evolution of the Goddard Profiling Algorithm to a Fully Parametric Scheme. – J. Atmos. Ocean. Technol. **32**, 2265–2280, DOI: 10.1175/JTECH-D-15-0039.1.

LE, M., V. CHANDRASEKAR, 2013: Precipitation Type Classification Method for Dual-Frequency Precipitation Radar (DPR) Onboard the GPM. – IEEE Transactions on Geoscience and Remote Sensing **51**, 1784–1790, DOI: 10.1109/TGRS.2012.2205698.

LE, M., V. CHANDRASEKAR, S. BISWAS, 2016: Evaluation and Validation of GPM Dual-Frequency Classification Module after Launch. – J. Atmos.d Ocean. Technol. **33**, 2699–2716, DOI: 10.1175/JTECH-D-15-0253.1.

LENGFELD, K., T. WINTERRATH, T. JUNGHÄNEL, M. HAFER, A. BECKER, 2019: Characteristic spatial extent of hourly and daily precipitation events in Germany derived from 16 years of radar data – Meteorol. Z. **28**, 363–378, DOI: 10.1127/metz/2019/0964.

LIAO, L., R. MENEGHINI, 2009: Validation of TRMM Precipitation Radar through Comparison of Its Multiyear Measurements with Ground-Based Radar. – J. Appl. Meteor. Climatol. **48**, 804–817, DOI: 10.1175/2008JAMC1974.1.

LIAO, L., R. MENEGHINI, A. TOKAY, 2014: Uncertainties of GPM DPR Rain Estimates Caused by DSD Parameterizations. – J. Appl. Meteor. Climatol. **53**, 2524–2537, DOI: 10.1175/JAMC-D-14-0003.1.

LOUF, V., A. PROTAT, R. WARREN, S. COLLIS, D. WOLFF, S. RAUNYIAR, C. JAKOB, W. PETERSEN, 2019: An Integrated Approach to Weather Radar Calibration and Monitoring Using Ground Clutter and Satellite Comparisons. – J. Atmos. Oceanic Technol. **36**, 17–39, DOI: 10.1175/JTECH-D-18-0007.1.

MENEGHINI, R., H. KIM, L. LIAO, J.A. JONES, J.M. KWIAT-KOWSKI, 2015: An Initial Assessment of the Surface Reference Technique Applied to Data from the Dual-Frequency Precipitation Radar (DPR) on the GPM Satellite. – J. Atmos. Ocean. Technol. **32**, 2281–2296, DOI: 10.1175/JTECH-D-15-0044.1.

MILAN, M., V. VENEMA, D. SCHÜTTEMEYER, C. SIMMER, 2008: Assimilation of radar and satellite data in mesoscale models: A physical initialization scheme. – Meteorol. Z. **17**, 887–902, DOI: 10.1127/0941-2948/2008/0340.

NAYAK, M.A., G. VILLARINI, A.A. BRADLEY, 2016: Atmospheric Rivers and Rainfall during NASA's Iowa Flood Studies (IFloodS) Campaign. – J. Hydrometeorol. **17**, 257–271, DOI: 10.1175/JHM-D-14-0185.1.

NEECK, S.P., R.K. KAKAR, A.A. AZARBARZIN, A.Y. HOU, 2014: Global Precipitation Measurement (GPM) launch, commissioning, and early operations. – In: MEYNART, R. S.P. NEECK, H. SHIMODA(Eds.): Sensors, Systems, and Next-Generation Satellites XVIII, volume 9241, 31–44. – International Society for Optics and Photonics, SPIE, DOI: 10.1117/12.2069868.

NICHOLSON, S.E., B. SOME, J. MCCOLLUM, E. NELKIN, D. KLOT-TER, Y. BERTE, B.M. DIALLO, I. GAYE, G. KPABEBA, O. NDIAYE, J.N. NOUKPOZOUNKOU, M.M. TANU, A. THIAM, A.A. TOURE, A.K. TRAORE, 2003: Validation of TRMM and Other Rainfall Estimates with a High-Density Gauge Dataset for West Africa. Part II: Validation of TRMM Rainfall Products. – J. Appl. Meteor. **42**, 1355–1368, DOI: 10.1175/1520-0450(2003)042<1355:VOTAOR>2.0.CO;2.

PARK, S., S.H. JUNG, G. LEE, 2015: Cross Validation of TRMM PR Reflectivity Profiles Using 3D Reflectivity Composite from the Ground-Based Radar Network over the Korean Peninsula. – J. Hydrometeorol. **16**, 668–687, DOI: 10.1175/JHM-D-14-0092.1.

PETRACCA, M., L.P. D'ADDERIO, F. PORCÙ, G. VULPIANI, S. SE-BASTIANELLI, S. PUCA, 2018: Validation of GPM Dual-Frequency Precipitation Radar (DPR) Rainfall Products over Italy. – J. Hydrometeorol. **19**, 907–925, DOI: 10.1175/JHM-D-17-0144.1.

PSCHEIDT, I., F. SENF, R. HEINZE, H. DENEKE, S. TRÖMEL, C. HOHENEGGER, 2019: How organized is deep convection over Germany? – Quart. J. Roy. Meteor. Soc. **145**, 2366–2384, DOI: 10.1002/qj.3552.

ROZANTE, J.R., D.S. MOREIRA, DE L.G.G. GONCALVES, D.A. VILA, 2010: Combining TRMM and Surface Observations of Precipitation: Technique and Validation over South America. – Wea. Forecast. **25**, 885–894, DOI: 10.1175/2010WAF2222325.1.

SCHWALLER, M.R., K.R. MORRIS, 2011: A Ground Validation Network for the Global Precipitation Measurement Mission. – J. Atmos. Ocean.Technol. **28**, 301–319, DOI: 10.1175/2010JTECHA1403.1.

SETO, S., T. IGUCHI, T. OKI, 2013: The Basic Performance of a Precipitation Retrieval Algorithm for the Global Precipitation Measurement Mission's Single/Dual-Frequency Radar Measurements. – IEEE Transactions on Geoscience and Remote Sensing **51**, 5239–5251, DOI: 10.1109/TGRS.2012.2231686.

SIMPSON, J., R.F. ADLER, G.R. NORTH, 1988: A Proposed Tropical Rainfall Measuring Mission (TRMM) Satellite – Bull. Amer. Meteor. Soc. **69**, 278–295, DOI: 10.1175/1520-0477(1988)069<0278:APTRMM>2.0.CO;2.

SKOFRONICK-JACKSON, G., W.A. PETERSEN, W. BERG, C. KIDD, E.F. STOCKER, D.B. KIRSCHBAUM, R. KAKAR, S.A. BRAUN, G.J. HUFFMAN, T. IGUCHI, P.E. KIRSTETTER, C. KUMMEROW, R. MENEGHINI, R. OKI, W.S. OLSON, Y.N. TAKAYABU, K. FURUKAWA, T. WILHEIT, 2017: The Global Precipitation Measurement (GPM) Mission for Science and Society. – Bull. Amer. Meteor. Soc. **98**, 1679–1695, DOI: 10.1175/BAMS-D-15-00306.1.

SPEIRS, P., M. GABELLA, A. BERNE, 2017: A Comparison between the GPM Dual-Frequency Precipitation Radar and Ground-Based Radar Precipitation Rate Estimates in the Swiss Alps and Plateau. – J. Hydrometeorol. **18**, 1247–1269, DOI: 10.1175/JHM-D-16-0085.1.

TAN, J., G.J. HUFFMAN, D.T. BOLVIN, E.J. NELKIN, 2019: IMERG V06: Changes to the Morphing Algorithm – J. Atmos. Ocean. Technol. **36**, 2471–2482, DOI: 10.1175/JTECH-D-19-0114.1.

WARREN, R.A., A. PROTAT, S.T. SIEMS, H.A. RAMSAY, V. LOUF, M.J. MANTON, T.A. KANE, 2018: Calibrating Ground-Based Radars against TRMM and GPM. – J. Atmos. Ocean. Technol. **35**, 323–346, DOI: 10.1175/JTECH-D-17-0128.1.

WATTERS, D., A. BATTAGLIA, K. MROZ, F. TRIDON, 2018: Validation of the GPM Version-5 Surface Rainfall Products over Great Britain and Ireland. – J. Hydrometeorol. **19**, 1617–1636, DOI: 10.1175/JHM-D-18-0051.1.

WINTERRATH, T., W. ROSENOW, E. WEIGL, 2012: On the DWD quantitative precipitation analysis and nowcasting system for real-time application in German flood risk management, Weather Radar and Hydrology. – IAHS Publ. **351**, 323–329.

WINTERRATH, T., C. BRENDEL, M. HAFER, T. JUNGHÄNEL, A. KLAMETH, E. WALAWENDER, E. WEIGL, A. BECKER, 2017: Erstellung einer radargestützten Niederschlagsklimatologie. – Berichte des Deutschen Wetterdienstes **251**, Deutscher Wetterdienst, Offenbach am Main.

WINTERRATH, T., C. BRENDEL, T. JUNGHÄNEL, A. KLAMETH, K. LENGFELD, E. WALAWENDER, E. WEIGL, M. HAFER, A. BECKER, 2018: An overview of the new radar-based precipitation climatology of the Deutscher Wetterdienst – data, methods, products. – Proc. 11th International Workshop on Precipitation in Urban Areas, Pontresina, Switzerland.

WOLFF, D.B., D.A. MARKS, E. AMITAI, D.S. SILBERSTEIN, B.L. FISHER, A. TOKAY, J. WANG, J.L. PIPPITT, 2005: Ground Validation for the Tropical Rainfall Measuring Mission (TRMM). – J. Atmos. Ocean. Technol.**22**, 365–380, DOI: 10.1175/JTECH1700.1.

WU, H., R.F. ADLER, Y. HONG, Y. TIAN, F. POLICELLI, 2012: Evaluation of Global Flood Detection Using Satellite-Based Rainfall and a Hydrologic Model. – J. Hydrometeorol.**13**, 1268–1284, DOI: 10.1175/JHM-D-11-087.1.